

# Millimetre-wave total internal reflection based computational imaging

L. E. Barr<sup>1,\*,+</sup>, P. Karlsen<sup>1,+</sup>, S. M. Hornett<sup>1</sup>, I. R. Hooper<sup>1</sup>, M. Mrnka<sup>1</sup>,  
C. R. Lawrence<sup>2</sup>, D. B. Phillips<sup>1</sup>, E. Hendry<sup>1</sup>

<sup>1</sup> School of Physics, University of Exeter, Exeter, EX4 4QL, UK

<sup>2</sup>QinetiQ, Cody Technology Park, Ively Road, Farnborough, GU14 0LX, UK

August 9, 2022

## Abstract

Imaging at millimetre wavelengths offers a promising route to the mapping of material properties in biological tissue. However, mm-wave radiation is difficult to control and detect, and the long wavelengths typically limit spatial resolution. In this work we demonstrate a computational mm-wave imaging system that operates under total internal reflection (TIR). A photo-activated spatial modulator in the near-field of the sample enables the evanescent field of a mm-wave beam to be dynamically patterned on a sub-wavelength scale. These fields are highly sensitive to both the complex refractive index and thickness of the sample, allowing images with these contrast mechanisms to be computationally reconstructed. We demonstrate the potential of our mm-wave imaging system by using it to image variations in sample thickness, map the local water content across proteinous and fatty regions of tissue, and image through a visibly opaque layer.

\*Corresponding author: l.barr@exeter.ac.uk

+These authors contributed equally to the work

Imaging in the Terahertz (THz) and mm-wave bands is highly appealing, yet it is a challenging region of the electromagnetic spectrum in which to work. There are many interesting and useful material responses to THz and mm-wave frequencies, and applications are beginning to emerge [1–3]. For example, THz and mm-waves are strongly absorbed by water, and so are capable of distinguishing water content in biological samples [4]. In addition, THz radiation is non-ionising, so is of particular interest for medical imaging. Recent examples of biological THz imaging include the study of cartilage from the knee [5], observation of the healing process of scar tissue [6], measuring the hydration of corneas [7] and imaging of water-dense cancers in breast tissue [8–10]. However, the inherent inhomogeneity of samples is a major challenge when imaging biological tissues [11]. THz/mm-wave imaging contrast is often dependent on both material response (e.g. the relative concentrations of fatty vs fibrous tissues) and the tissue depth [9].

A second challenge is the poor sensitivity of detectors in the THz and mm-wave spectral bands, as the low energies carried by photons makes their control and detection extremely demanding. The most sensitive detectors require deep cryogenic cooling, which is problematic for arrays, where the individual signals from thousands of detectors must be acquired per frame. Cheap and reliable detector arrays in the THz and mm-wave spectral bands have yet to be developed. In the near-field, scanning probe techniques have been applied to capture sub-wavelength THz images of surface features. However weak signals emanating from the probe, which is sub-diffraction limited in scale, coupled with noisy detectors, result in lengthy measurement times [12–14].

Emerging computational imaging techniques offer a potential way forward by redefining our understanding of how images can be recorded. Such systems do not form an image directly, but offload aspects of the image formation process to a computer. ‘Single-pixel’ computational imaging systems circumvent the need for detector arrays, and boost the magnitude of near-field measurements by recording signals from many locations at once. These systems encode spatial information in the temporal dimension, enabling operation at wavelengths where multi-pixel sensors are challenging to fabricate, prohibitively expensive, or simply do not exist [15]. Images are reconstructed from measurements using a single-element detector, which itself records only the total incident intensity, in conjunction with a spatial light modulator (SLM). The SLM spatially modulates (i.e. varies) the intensity of light, and so enables sequential illumination of the target object with a series of patterned light fields, each of which probes a different subset of the spatial information in the scene. Recently there have been several demonstrations of deeply sub-wavelength single-pixel transmission imaging at THz frequencies [16–19].

In this work we demonstrate a new form of sub-wavelength resolution millimetre-wave computational imaging system. We refer to our approach as a type of total internal reflection (TIR) imaging: in the absence of loss we anticipate perfect reflection, while lossy samples reduce reflection producing sample dependent image contrast. Our device is based upon a bespoke optically addressed mm-wave spatial modulator, integrated with a dove prism in a TIR geometry. This allows dynamic patterning of the evanescent mm-wave field probing the underside of potentially non-transmissive objects [20], opening up access to a range of new types of sample, including thick biological tissues. In contrast with previous single-pixel THz imagers, which typically produce an absorption image of a thin sample in transmission mode, our total internal reflection geometry gives access to a richer vein of information about the sample: the reflected signal is highly sensitive to both material properties and sample thickness. In addition, while optical frequency total internal reflection microscopy penetrates fractions of a micron into samples [21], the scaling with wavelength means that our mm-wave system is capable of probing millimetric distances into samples - distances relevant, for example, to the determination of the thickness of structural tissue changes found in cancerous samples [22], or the study of the layered structure of the skin [23].

Critical to the performance of our imaging system is the mm-wave spatial modulator, and we describe in detail how this has been tuned for use at mm-wavelengths. This optimisation balances the resolution, frame-rate and contrast of the modulator. Optical modulation in the TIR geometry is also efficient, circumventing the requirement for high intensity femtosecond-pulse optical pump beams [24, 25], vastly simplifying the experimental set-up in comparison with earlier work [26–28], removing unwanted heating of sensitive samples,

and reducing optical noise. We show that our TIR based imaging system offers a new way forward to simultaneously image and measure the thickness of biological samples. To interpret our images throughout our study, we compare them with a transfer matrix based model describing expected levels of reflection as a function of frequency, incident angle and material parameters of the sample. We investigate the effect of the sample characteristics on image formation, and experimentally show that the measured signal encodes information about both the material and the film thickness. In our proof-of-principle experiments, we show that TIR mm-wave images reveal regions of fat and protein in porcine tissue samples, highlighting the system as a good candidate for imaging water-dense samples such as cancer tumours. We also demonstrate that it is possible to detect objects embedded within a thick optically-opaque material, by imaging a metal target on the far side of a fatty layer of tissue. While at present we have implemented this technique for mm-wave imaging, the principles described here could be broadly applied from GHz through to THz frequencies.

### Building a mm-wave TIR imaging system

Our TIR imaging system is based on all-optical modulation (known as photo-modulation), where a visible or near-IR light source is used to change the transparency of a photo-active medium to low frequency radiation. This approach is often chosen because it is relatively simple to implement, can be very fast and can operate over a broad range of mm-wave and THz frequencies [29, 30].

Figure 1(a) shows a schematic of our TIR imaging system. An IMPATT (IMPact ionization Avalanche Transit-Time) diode source (*TeraSense*, power 30 mW) produces a continuous wave with a frequency of  $140 \text{ GHz} \pm 1 \text{ MHz}$  (a wavelength of around 2.15 mm). This passes through a dove prism made of a polymer, TPX (polymethylpentene) [31], which is transparent to both optical and GHz/THz radiation, with a refractive index of 1.58 and low loss (a tangent of  $8 \times 10^{-4}$ ) at 140 GHz. The mm-wave spatial modulator is formed from a  $390 \mu\text{m}$  thick photo-active silicon wafer, placed on top of the prism, with a thin layer of immersion oil (refractive index of 1.513) between the wafer and prism to prevent air-gaps. The sample is then placed on top of the silicon wafer: its proximity to the mm-wave modulator means we can pattern the mm-wave on a sub-wavelength scale, as the fields at the surface of the silicon do not diffract. The mm-wave components that are totally internally reflected at the silicon-air interface are detected by an ultrafast THz detector (*TeraSense*).

Before photo-activation, the silicon wafer is largely transparent to mm-wave radiation. When illuminated at an angle of incidence greater than the critical angle, mm-waves are totally internally reflected from the silicon-air interface. Upon illumination of the silicon wafer with visible light, electron-hole pair photo-excitation increases the mm-wave absorption and so reduces mm-wave reflection. Therefore, by projecting optical binary intensity patterns onto the silicon wafer using light from a LED pump beam (*Thorlabs SOLIS*, wavelength  $623 \pm 5 \text{ nm}$ , power 4.7 W) patterned with a digital micro-mirror device (DMD, *Vialux*), we are able to spatially control which areas of the modulator are more reflective to mm-wave radiation. In this way, the pattern in the optical pump beam is dynamically imprinted onto the mm-wave field bathing the sample, enabling single-pixel imaging to be performed. The projected optical binary patterns are drawn from the Hadamard basis. This basis yields reconstructed images with significantly higher signal-to-noise ratio (SNR) compared to simple raster scanning of a transparent (or absorbing) window, and the SNR is uniformly

distributed over the reconstructed image as the set is orthogonal [32, 33]. Detail of the image reconstruction can be found in section 3.1 of the supplementary material. Our data acquisition rate is nominally 2 kHz, limited by the lifetime of the charge carriers in the silicon wafer, which, for  $64 \times 64 = 4096$  pixels with sufficient signal to observe features in the samples, results in each image taking around 4 seconds to collect. To allow for low noise image analysis, the images presented below have been averaged for several minutes (see section supplementary for a full analysis), which equates to 1 minute 22 seconds of exposure when omitting programming wait times.

The penetration length of the evanescent field in air,  $L$ , depends on both the incident angle of the mm-wave beam and its frequency, as shown in Fig. 1(b).  $L$  is maximised for low frequencies (i.e. longer wavelengths) and angles very close to the critical angle (white dotted line). These dependencies allow  $L$  to be tuned to match the sample characteristics. In this work we elected to image at a frequency of 140 GHz and incident angle of  $49^\circ$  (denoted by the red circle in Fig. 1 (b)), giving a penetration depth in air of  $\sim 300 \mu\text{m}$ .

### Responsivity to sample thickness

THz time domain measurement is often used as a route to film thickness determination, either using time of flight approaches [34, 35] or through spectral analysis [36, 37]. These techniques achieve thickness measurements of exceptionally high accuracy - approaching microns. However, to achieve high depth sensitivity requires illumination with collimated beams (i.e. only weakly focused beams with a narrow angular spectrum). This requirement limits the lateral spatial resolution of these methods, as high depth sensitivity is not compatible with the strong focusing necessary to achieve high lateral resolution. This trade-off is also inherent in total internal reflection imaging techniques that have been demonstrated to date [38, 39]. Therefore, the low lateral resolution of these approaches presents a drawback when imaging inhomogeneous samples typical in biological systems [11]. The trade-off between depth sensitivity and lateral spatial resolution means that time domain techniques have been most successfully employed to investigate homogeneous samples such as polymer films [40] or crystalline pallets [41]. In contrast, our TIR approach decouples depth sensitivity from lateral resolution. Below, we show that our technique enables determination of sample thickness with significantly sub-wavelength accuracy, while also retaining high lateral resolution.

When a layer of material is placed on top of the silicon wafer, the intensity of the mm-wave beam reflected back into the detector depends upon both the complex refractive index and thickness of the layer. If the refractive index of the material is less than that of the prism, one expects evanescent fields at the silicon-sample boundary that are sensitive to the properties of the sample [20]. If the sample has an index higher than the prism, one breaks the total internal reflection condition at the silicon-sample interface, allowing a propagating wave to interrogate the sample layer.

To study these effects we image a step in a polymer sample of known height and permittivity ( $3.5 + 0.53i$ ), and compare the image to the modulation predicted by simulation [42]. The sample under investigation is created by layering cellulose from tape to create films of different thicknesses. Reconstructed images are spatial maps of  $\delta r(x, y)$ , which is the difference in reflected signal at each spatial location  $(x, y)$ , as the mm-wave modulator is switched from its Off (dark) to On (i.e. photo-activated) state. Figure 2(a) shows the predicted level

of mm-wave modulation  $\delta r$  as a function of incident angle and sample thicknesses. Circles (1) and (2) indicate the expected signals at thicknesses of  $350 \pm 10 \mu\text{m}$  and  $570 \pm 10 \mu\text{m}$ . Figure 2(b) shows experimentally obtained visible (left panel) and mm-wave (right panel) images of the polymer step.

One intriguing feature of Fig. 2 is that the sign of  $\delta r$  changes as a function thickness.  $\delta r > 0$  indicates a decrease in reflection of mm-wave radiation on photo-excitation of the silicon wafer, while  $\delta r < 0$  indicates an increase.  $\delta r < 0$  is somewhat unexpected: why would an introduction of absorption into the silicon layer lead to an *increase* in the level of reflected radiation? This surprising effect arises due to an optimal matching condition between the absorption and radiative loss channels of the system, which defines critical coupling conditions [43]. This is similar to an effect observed for plasmonic cavities [44, 45], and arises here due to a Fabry-Perot resonance present in the sample itself. It is clear that the change in sign of  $\delta r$  is both predicted in our wave modelling (Fig. 2(a)) and observed in experiment (Fig. 2(b)). However, the negative signals measured in experiment have a larger magnitude than those predicted from our modelling: we suspect this arises due to small air gaps in between cellulose layers changing the matching condition. Nevertheless, as demonstrated, an image contrast ( $\delta r$ ) which *varies in sign* upon a change in sample thickness of an order of magnitude smaller than the wavelength, has significant measurement potential, especially for challenging samples made from malleable and soft materials.

### Imaging biological tissue

We now demonstrate imaging of inhomogeneous biological tissues using our mm-wave TIR imaging system. The sample is a  $750 \pm 250 \mu\text{m}$  thick piece of sliced porcine tissue, which exhibits strong spatial variation in properties, varying from fatty to protein rich regions. While one can expect a high degree of variation in the complex permittivities of biological tissues (see section 4.4 of the supplementary material) [9, 22, 46, 47], for now in our model we assume protein and fat are described by  $\epsilon_{\text{fat}} = 2.89 + 0.64i$  and  $\epsilon_{\text{protein}} = 8.63 + 11.20i$ , taken from reference [48]. Using these values, Fig. 3(a) shows modelling of reflected mm-wave signal when a layer of fat or protein is placed on top of the wafer, as a function of incident angle, for both photo-activated ( $220 \text{ Wm}^{-2}$ ) and dark silicon. We show modelling results for three different thicknesses of material within the experimentally measured range.

Our model indicates that materials with high losses, such as protein, do not exhibit strong variation in  $\delta r$  as sample thickness changes, due to the strong absorption of the mm-wave beam. We show the dependency of reflection on incident angle for a single thickness of protein tissue ( $700 \mu\text{m}$ , blue plot) in Fig. 3(a). We also see that the difference in predictions for a illuminated and non-illuminated modulator is very small (i.e.  $\delta r$  is expected to be small) for protein tissue. There are two factors which determine this: firstly the absorption of the mm-wave is higher in protein than in fat, due to its higher water content; secondly, the real part of the refractive index of protein is close to that of silicon, and therefore a significant drop in the reflection is expected in this case. Fatty tissue, on the other hand, has a much lower water content, and hence absorption is lower. We predict fatty tissue will exhibit a strong variation of  $\delta r$  on sample thickness. This is shown in the red and yellow plots in Fig. 3(a), which show reflection as a function of incident angle for two thicknesses ( $680 \mu\text{m}$ , yellow plot, and  $810 \mu\text{m}$ , red plot,). Here we see that  $\delta r$ , the difference between dashed and solid lines, is expected to change sign when passing through the minimum in reflection at

around 50 degrees (60 degrees) for a thickness of 680 $\mu\text{m}$  (810  $\mu\text{m}$ ). We therefore see a range of angles, marked by the grey region, where we expect signal to be completely opposite in sign for a thickness difference of just 130 $\mu\text{m}$  (i.e. just 5% of the mm-wave wavelength).

In Figs. 3(b) and (c) we present mm-wave images of two different samples of porcine tissue: one with a large region of fat well separated from the protein (b), and one with filaments of fat on the scale of the imaging wavelength running through the protein (c). In both images, the regions of fat and protein are clearly distinguishable, as seen by comparison to the optical images on the left. As predicted,  $\delta r$  is close to zero within regions of protein in both Figs. 3(b) and (c). Approximate measurements using a set of Vernier Calipers gave the thickness of fatty regions in Fig. 3(b) to be  $810 \pm 200 \mu\text{m}$ , while the thickness of the fat in Fig. 3(c) was estimated to be  $680 \pm 150 \mu\text{m}$ . As predicted by our model, the measured  $\delta r$  of fatty tissue regions in each image have opposite sign. We present further simulations in section 4.3 of the supplementary material that illustrate this great sensitivity to permittivity and sample thickness. The low absorption of fat also allows us to image objects behind layers of fatty tissue. This is shown experimentally in section 4.6 of the supplementary material - demonstrating potential for imaging through visibly opaque fatty tissues.

### Exploring physical limitations of the system

There are several inter-related factors which limit the performance of our TIR computational imaging system. Conventional diffraction limited imaging systems can reach resolutions of  $\sim \lambda/2\text{NA}$ , where NA is the numerical aperture of the focusing rays. To achieve high depth sensitivity one requires illumination with near-collimated mm-waves: our system has a mm-wave NA = 0.06, similar to NAs used in both time of flight systems [34, 35] and previous TIR imaging systems [38, 39]. An NA = 0.06 corresponds to an expected diffraction limited resolution  $\sim 1.8 \text{ cm}$  for 140 GHz - this demonstrates the trade off between lateral and depth resolution normally inherent to both time of flight and TIR approaches. However, in our design, the in-plane lateral resolution of images is determined by the wavelength of the optical pump beam, and charge carrier diffusion within the silicon wafer (i.e. how far the charge carriers drift thus blurring the optical pump pattern), rather than the wavelength of the mm-wave beam, meaning sub-diffraction limited imaging is possible. Figure 4(a) shows how the diffusion of charge carriers in the silicon depends on their effective lifetime. Reconstructed images inherit the same level of blurring as the patterning of the mm-wave field has undergone due to drift of charge carriers. In this case the point spread function of the system is governed by the drift-induced long range correlations in the mm-wave field patterns used to probe the object [49]. The lifetime of the wafer chosen for our experiments is 75  $\mu\text{s}$  (float zone silicon bought from Siltronic, dark resistivity = 5  $\text{k}\Omega$ , thickness = 390  $\mu\text{m}$ , 120 nm of  $\text{SiO}_2$  passivation; see section 2.4 of the supplementary material for more information). A lifetime of 75  $\mu\text{s}$  leads to a diffusion length of 350  $\mu\text{m}$ , and a lateral resolution of twice this value i.e. 700  $\mu\text{m}$ , which agrees with the resolutions observed in our images.

There is also scope to achieve lateral resolutions far below our experimental limit by reducing the effective carrier lifetime of the modulator [42]. However Fig. 4(a) also shows that, for a given optical pump power, decreasing the carrier lifetime simultaneously decreases the reflection modulation depth,  $\text{MD} = R_{\text{dark}} - R_{\text{illum}}$ , which depends on the reflected intensity of the mm-wave when the silicon is dark,  $R_{\text{dark}}$ , and illuminated,  $R_{\text{illum}}$ . Ultimately, MD is a function of carrier lifetime, as one can achieve a higher photoconductivity for longer

lifetimes (see section 2.5 of the supplementary material). For our experiment, a lifetime of 75  $\mu\text{s}$  provided a reasonable trade off between resolution and MD, while higher MD comes at a cost of lower imaging resolution. Conversely, for applications where long imaging times and averaging are possible, one could trade SNR in return for significantly higher imaging resolution.

There are other parameters we can tune to ensure that MD is maximised without compromising on the speed and resolution of imaging - namely the incident angle, wafer thickness and frequency. In Fig. 4(b) we show the numerically calculated MD as a function of incident angle and silicon wafer thickness, on a TPX-silicon-air stack (calculated here for TE polarisation and 140 GHz with an excitation intensity of  $220 \text{ Wm}^{-2}$  and excitation wavelength of 623 nm for a silicon wafer with effective charge carrier lifetime  $\tau_{\text{eff}} = 75 \mu\text{s}$ ). The inset shows the reflected mm-wave intensity for dark and illuminated states, for a 390  $\mu\text{m}$  thick wafer. For a stack of TPX-silicon-air we predict the onset of TIR for a critical angle of  $39.3^\circ$ . For angles beyond  $\theta_{\text{crit}}$  the modulation is around an order of magnitude larger than that achieved at normal incidence. The incident angle that provides the largest modulation is near grazing incidence. However, as discussed earlier, angles closer to the critical angle give evanescent fields which penetrate further into low index samples (see Fig. 1(b)), so we opt for a lower angle of  $49^\circ$ , marked by the red circle, where the penetration length of the field is around 300  $\mu\text{m}$  in air.

It is also clear from Fig. 4(b) that the modulation is dependent on the thickness of the silicon wafer. This arises due to a cavity resonance in the wafer, as reported in [42], which gives an increased modulation when the wafer thickness is equal to a half-integer multiple of the wavelength in silicon. For a mm-wave frequency of 140 GHz, we choose a wafer that is 390  $\mu\text{m}$  thick. For this work we were limited to commercially available silicon wafers, however despite this we were able to select a suitable set of parameters for a proof of principle demonstration of our TIR system.

## Conclusions

In conclusion, we have demonstrated a computational mm-wave imaging system based on a silicon photo-modulator in a total internal reflection geometry. In comparison with previously demonstrated THz and mm-wave computational imaging systems [26, 37, 38], our design exhibits a high pixels-per-second rate of several kHz, which gives a resolution-dependent frame rate of a few seconds. In section 3.3 of the supplementary material we demonstrate the trade-off between SNR in images and modulation rate in our current setup. Our TIR system is also cheaper and more compact than previous work, as it circumvents the need for femtosecond-pulsed lasers.

Through simulations and experiments we have shown how the field present in the sample, and thus the magnitude of the reflected signal, is highly sensitive to both the complex refractive index, and thickness of the sample. The system possesses a number of interdependent parameters which can be tuned to match sample characteristics. These include the contrast, response time and lateral resolution of the mm-wave modulator, the penetration depth of the evanescent field, and incident angle and frequency of mm-wave radiation.

In particular, the penetration depth is dependent on both incident angle and mm-wave frequency. This points to an intriguing avenue for future development of the system. By capturing several images at a range of incident angles and frequencies, it is possible to de-

couple material parameters from layer thickness, and so independently recover these sample properties simultaneously. Section 4.5 of the supplementary material details modelling that demonstrates this principle for some simple cases. In the future it may be possible to extend this approach to recover tomographic images of more complex samples which exhibit strong inhomogeneity in all three dimensions. Together, we believe these features point towards many potential applications of mm-wave TIR imaging in, for example, the medical, art conservation and food industries.

### Data availability

All data that support the findings of this study are available from the University of Exeter’s institutional repository, [link].

## References

- [1] Ritesh Jain, Janusz Grzyb, Ullrich R Pfeiffer, and Senior Member. Terahertz Light-Field Imaging. *IEEE Transactions on Terahertz Science and Technology*, 6(5):649–657, 2016.
- [2] Ashish Y. Pawar, Deepak D. Sonawane, Kiran B. Erande, and Deelip V. Derle. Terahertz technology and its applications. *Drug Invention Today*, 5(2):157–163, 2013.
- [3] Aurele Joseph Louis Adam. Review of near-field Terahertz measurement methods and their applications: How to achieve sub-wavelength resolution at THz frequencies. *Journal of Infrared, Millimeter, and Terahertz Waves*, 32(8-9):976–1019, 2011.
- [4] Yuezhi He, Kai Liu, Corinna Au, Qiushuo Sun, Edward P.J. Parrott, and Emma Pickwell-MacPherson. Determination of terahertz permittivity of dehydrated biological samples. *Physics in Medicine and Biology*, 62(23):8882–8893, 2017.
- [5] Rayko I. Stantchev, Jessica C. Mansfield, Ryan S. Edginton, Peter Hobson, Francesca Palombo, and Euan Hendry. Subwavelength hyperspectral THz studies of articular cartilage. *Scientific Reports*, 8(1):1–8, 2018.
- [6] Shuting Fan, Benjamin S.Y. Ung, Edward P.J. Parrott, Vincent P. Wallace, and Emma Pickwell-MacPherson. In vivo terahertz reflection imaging of human scars during and after the healing process. *Journal of Biophotonics*, 10(9):1143–1151, 2017.
- [7] Zachary D. Taylor, James Garritano, Shijun Sung, Neha Bajwa, David B. Bennet, Bryan Nowroozi, Priyamvada Tewari, James W. Sayre, and Jean-Pierre Hubschman. THz and mm-Wave Sensing of Corneal Tissue Water Content: In Vivo Sensing and Imaging Results. *HPS Public Access*, 20(1):48–55, 2017.
- [8] Calcin Yu, Shuting Fan, Yiwen Sun, and Emma Pickwell-MacPherson. The potential of terahertz imaging for cancer diagnosis: A review of investigations to date. *Quantitative Imaging in Medicine and Surgery*, 2(1):33–45, 2012.

- [9] Philip C. Ashworth, Emma Pickwell-MacPherson, Elena Provenzano, Sarah E. Pinder, Anand D. Purushotham, Michael Pepper, and Vincent P. Wallace. Terahertz pulsed spectroscopy of freshly excised human breast cancer. *Optics Express*, 17(15):12444, 2009.
- [10] Anthony J. Fitzgerald, Emma Pickwell-MacPherson, and Vincent P. Wallace. Use of finite difference time domain simulations and debye theory for modelling the terahertz reflection response of normal and tumour breast tissue. *PLoS ONE*, 9(7):1–9, 2014.
- [11] Tyler C. Bowman, Magda El-Shenawee, and Lucas K. Campbell. Terahertz Imaging of Excised Breast Tumor Tissue on Paraffin Sections. *IEEE Transactions on Antennas and Propagation*, 63(5):2088–2097, 2015.
- [12] Jiayu Zhao, Wei Chu, Lanjun Guo, Zhi Wang, Jing Yang, Weiwei Liu, Ya Cheng, and Zhizhan Xu. Terahertz imaging with sub-wavelength resolution by femtosecond laser filament in air. *Scientific Reports*, 4(3880):1–7, 2014.
- [13] M. Eisele, T. L. Cocker, M. A. Huber, M. Plankl, L. Viti, D. Ercolani, L. Sorba, M. S. Vitiello, and R. Huber. Ultrafast multi-terahertz nano-spectroscopy with sub-cycle temporal resolution. *Nature Photonics*, 8(11):841–845, 2014.
- [14] F Blanchard, A Doi, T Tanaka, H Hirori, H Tanaka, and Y Kadoya. Real-time terahertz near-field microscope. *Optics Express*, 19(9):3523–3525, 2011.
- [15] Erwin Hack, Lorenzo Valzania, Gregory Gäumann, Mostafa Shalaby, Christoph P. Hauri, and Peter Zolliker. Comparison of thermal detector arrays for offaxis THz holography and realtime THz imaging. *Sensors (Switzerland)*, 16(2):1–11, 2016.
- [16] Wai Lam Chan, Jason Deibel, and Daniel M. Mittleman. Imaging with terahertz radiation. *Reports on Progress in Physics*, 70(8):1325–1379, 2007.
- [17] David Shrekenhamer, Claire M. Watts, and Willie J. Padilla. Terahertz single pixel imaging with an optically controlled dynamic spatial light modulator. *Optics Express*, 21(10):12507, 2013.
- [18] Syed An Nazmus Saqueeb and Kubilay Sertel. Phase-sensitive THz imaging using single-pixel intensity-only measurements. *2016 IEEE Antennas and Propagation Society International Symposium, APSURSI 2016 - Proceedings*, 6(6):1065–1066, 2016.
- [19] Samuel M. Hornett, Rayko I. Stantchev, Martha Z. Vardaki, Chris Beckerleg, and Euan Hendry. Subwavelength Terahertz Imaging of Graphene Photoconductivity. *Nano Letters*, 16(11):7019–7024, 2016.
- [20] M. L. Martin-Fernandez, C. J. Tynan, and S. E D Webb. A ‘pocket guide’ to total internal reflection fluorescence. *Journal of Microscopy*, 252(1):16–22, 2013.
- [21] D. Axelrod. Total Internal Reflection Fluorescence Microscopy. *Encyclopedia of Cell Biology*, 2(2):62–69, 2016.

- [22] Tyler Bowman, Magda El-Shenawee, and Lucas K. Campbell. Terahertz transmission vs reflection imaging and model-based characterization for excised breast carcinomas. *Biomedical Optics Express*, 7(9):3756, 2016.
- [23] Emma Pickwell, B. E. Cole, A. J. Fitzgerald, M. Pepper, and V. P. Wallace. In vivo study of human skin using pulsed terahertz radiation. *Physics in Medicine and Biology*, 49(9):1595–1607, 2004.
- [24] Xudong Liu, Edward P.J. Parrott, Benjamin S.Y. Ung, and Emma Pickwell-MacPherson. Exploiting total internal reflection geometry for efficient optical modulation of terahertz light. *APL Photonics*, 1(7):076103, 2016.
- [25] Rayko Ivanov Stantchev, Xiao Yu, Thierry Blu, and Emma Pickwell-macpherson. Real-time terahertz imaging with a single-pixel detector. *Nature Communications*, 1(11):2535, 2020.
- [26] Rayko Ivanov Stantchev, Baoqing Sun, Sam M. Hornett, Peter A. Hobson, Graham M. Gibson, Miles J. Padgett, and Euan Hendry. Noninvasive, near-field terahertz imaging of hidden objects using a single-pixel detector. *Science Advances*, 2(6):1600190, 2016.
- [27] Tatsuo Nozokido, Hiroaki Minamide, and Koji Mizuno. Modulation of Submillimeter Wave Radiation by Laser-Produced Free Carriers in Semiconductors. *Electronics and Communications in Japan*, 80(6):259–266, 1997.
- [28] Takanori Okada and Koichiro Tanaka. Photo-designed terahertz devices. *Scientific Reports*, 1(121):1–5, 2011.
- [29] Yang Bai, Ting Bu, Kejian Chen, and Songlin Zhuang. Review about the Optical-Controlled Terahertz Waves Modulator. *Applied Spectroscopy Reviews*, 50(9):707–727, 2015.
- [30] Marco Rahm, Jiu Sheng Li, and Willie J. Padilla. THz wave modulators: A brief review on different modulation techniques. *Journal of Infrared, Millimeter, and Terahertz Waves*, 34(1):1–27, 2013.
- [31] Chemicals Mitsui America Inc. TPX Datasheet, 2019.
- [32] N J Sloane and M Harwit. Masks for Hadamard transform optics, and weighing designs. *Applied optics*, 15(1):107–114, 1976.
- [33] J. A. Decker. Hadamard Transform Image Scanning. *Applied Optics*, 9(6):1392, 1970.
- [34] Hua Zhong, Jingzhou Xu, Xu Xie, Tao Yuan, Ron Reightler, Eric Madaras, and Xi Cheng Zhang. Nondestructive defect identification with terahertz time-of-flight tomography. *IEEE Sensors Journal*, 5(2):203–207, 2005.
- [35] E. Abraham, A. Younus, J. C. Delagnes, and P. Mounaix. Non-invasive investigation of art paintings by terahertz imaging. *Applied Physics A: Materials Science and Processing*, 100(3):585–590, 2010.

- [36] Jon L. Johnson, Timothy D. Dorney, and Daniel M. Mittleman. Enhanced depth resolution in terahertz imaging using phase-shift interferometry. *Applied Physics Letters*, 78(6):835–837, 2001.
- [37] Tadao Nagatsuma, Toshiyuki Ikee, and Hiroki Nishii. Terahertz imaging based on optical coherence tomography. *ICECom 2013 - Conference Proceedings: 21st International Conference on Applied Electromagnetics and Communications*, 2(4):64–69, 2013.
- [38] Antoine Wojdyla and Guilhem Gallot. Attenuated internal reflection terahertz imaging. *Optics Letters*, 38(2):112–114, 2013.
- [39] Marianne Grognot and Guilhem Gallot. Quantitative measurement of permeabilization of living cells by terahertz attenuated total reflection. *Applied Physics Letters*, 107(1):103702, 2015.
- [40] Lin Chen, Yifan Ge, Xiaofei Zang, Jingya Xie, Li Ding, Alexei V. Balakin, Alexander P. Shkurinov, and Yiming Zhu. Tunable Phase Transition via Radiative Loss Controlling in a Terahertz Attenuated Total Reflection-Based Metasurface. *IEEE Transactions on Terahertz Science and Technology*, 9(6):643–650, 2019.
- [41] Dahi Ghareab Abdelsalam Ibrahim, Safaa K.H. Khalil, H. H.A. Sherif, and M. M. Elokher. Multilayer film thickness measurement using ultrafast terahertz pulsed imaging. *Journal of Physics Communications*, 3(6), 2019.
- [42] I. R. Hooper, N. E. Grant, L. E. Barr, S. M. Hornett, J. D. Murphy, and E. Hendry. High efficiency photomodulators for millimeter wave and THz radiation. *Scientific Reports*, 9(1):1–10, 2019.
- [43] Herman A. Haus. *Waves and fields in optoelectronics*. Prentice-Hall Inc., Englewood Cliffs, New Jersey, New Jersey, 1984.
- [44] S. Herminghaus, M. Klopffleisch, and H. J. Schmidt. Attenuated total reflectance as a quantum interference phenomenon. *Optics Letters*, 19(4):293, 1994.
- [45] H. Raether. *Surface Plasmons on Smooth and Rough Surfaces and on Gratings*. Springer-Verlag, Berlin, 1 edition, 1988.
- [46] Yiwen Sun, Bernd M. Fischer, and Emma Pickwell-MacPherson. Effects of formalin fixing on the terahertz properties of biological tissues. *Journal of Biomedical Optics*, 14(6):064017, 2009.
- [47] Yiwen Sun. A promising diagnostic method: Terahertz pulsed imaging and spectroscopy. *World Journal of Radiology*, 3(3):55, 2011.
- [48] Camelia Gabriel. Compilation of the Dielectric Properties of Body Tissues at RF and Microwave Frequencies. Technical report, 1996.
- [49] D. B. Phillips, Ruiqing He, Qian Chen, G. M. Gibson, and M. J. Padgett. Non-diffractive computational ghost imaging. *Optics Express*, 24(13):14172, 2016.

## **Acknowledgements**

L.E.B and I.R.H. acknowledge financial support from the Engineering and Physical Sciences Research Council of the United Kingdom (EPSRC UK) and QinetiQ Ltd. via the TEAM-A Prosperity Partnership (Grant No. EP/R004781/1). D.B.P acknowledges financial support from the Royal Academy of Engineering (UK) and the European Research Council (Grant No. 804626). E.H. and M.M acknowledge financial support from the EPSRC UK (Grant No. EP/S036466/1). E.H. and D.B.P also acknowledge financial support from the EPSRC UK (Grant No. QuantIC EP/M01326X/1).

## **Author contributions**

L.E.B. collected the images, performed the simulations, interpreted the results and prepared the manuscript. P.K built the imaging system. S.M.H. built the imaging system and assisted with simulations. I.R.H. assisted with simulations and interpretation. M.M. assisted with interpretation. C.R.L. supervised the project. D.B.P provided support on computational imaging, assisted with interpretation and supervised the project. E.H. devised the experiment, assisted with interpretation and supervised the project. All authors edited the manuscript.

## **Competing interests**

The authors declare no competing interests.

## **Additional information**

Supplementary information is available for this paper at [link].

Correspondence and requests for information should be addressed to L.E.B.

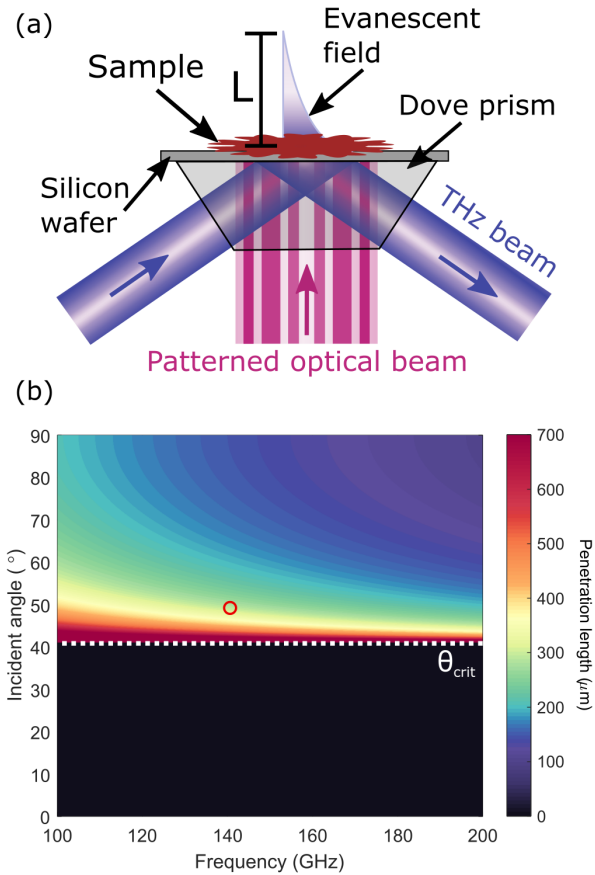


**Fig. 1.** (a) Schematic showing mm-wave modulator using total internal reflection. (b) Calculated penetration length of evanescent fields,  $L$ , at the silicon-air interface for a range of frequencies and angles of incidence. The 390  $\mu\text{m}$  thick silicon wafer has a permittivity of  $11.7 + 0.003i$ , and the prism medium has a permittivity of 2.49. The white dashed line shows the critical angle, below which there are no evanescent fields, and the red circle denotes the selected experimental parameters.

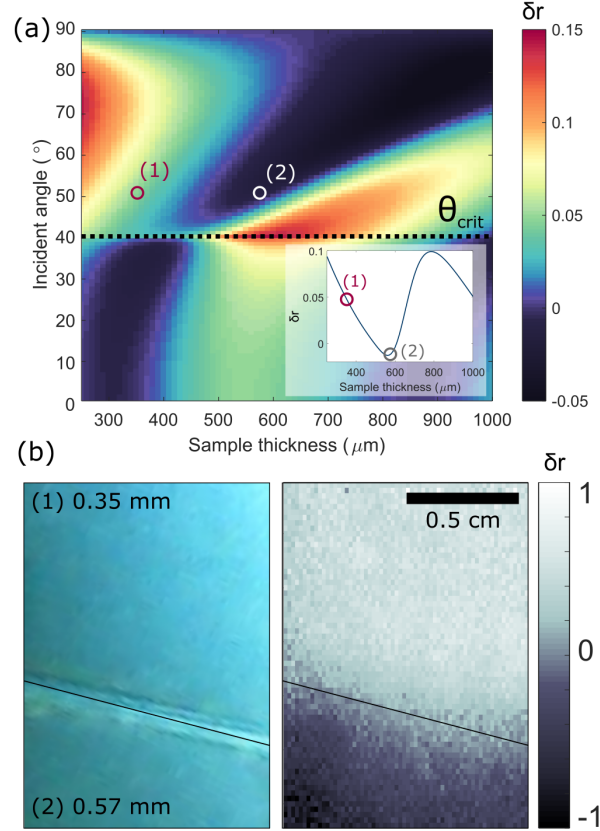


**Fig. 2.** (a) Calculated  $\delta r$  when a sample of permittivity  $3.5 + 0.525i$  is present on top of the silicon wafer, as a function of sample thickness and incident angle of the mm-wave beam. The inset shows a slice through the plot at  $50^\circ$  incidence. Results are calculated at 140 GHz frequency, and an incident photoexcitation wavelength of 623 nm and power of  $220 \text{ Wm}^{-2}$  when illuminated, and  $0 \text{ Wm}^{-2}$  when dark. The silicon wafer has a thickness of  $390 \mu\text{m}$  and a charge carrier lifetime of  $75 \mu\text{s}$ . The critical angle is marked by the dotted black line. The red and white (inset: grey) circles (1) and (2) denote the parameters corresponding to the image in (b). (b) Optical (left) and mm-wave (right) images of a polymer sample with regions of two different thicknesses.

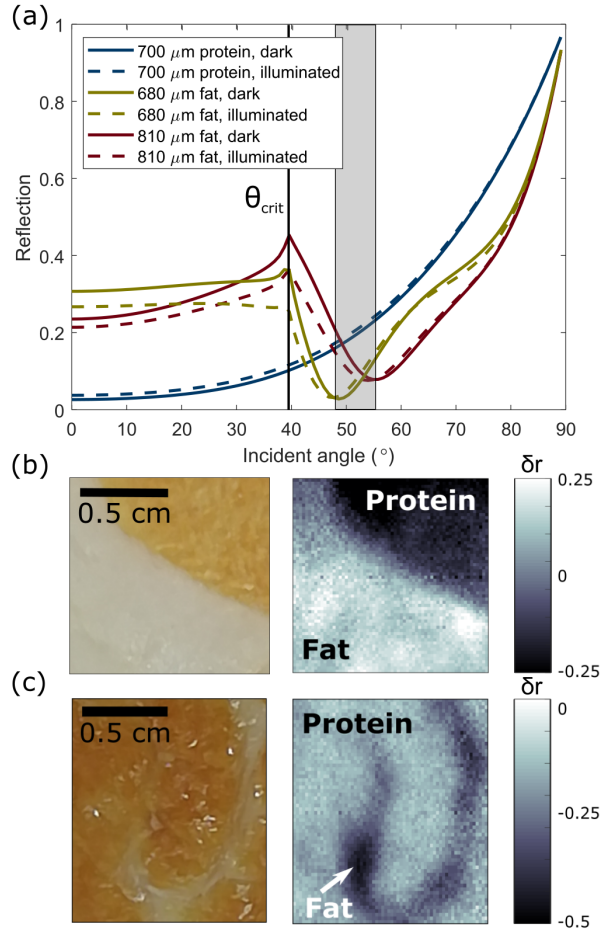


**Fig. 3.** (a) Calculated reflection of a TE polarised mm-wave signal at 140 GHz when various biological tissues are placed on top of the silicon wafer, when the silicon is dark (solid lines) or illuminated (dashed lines) with a photoexcitation beam of  $220 \text{ Wm}^{-2}$  at 623 nm wavelength. The silicon wafer has a thickness of  $390 \mu\text{m}$  and a charge carrier lifetime of  $75 \mu\text{s}$ . The critical angle ( $\theta_{\text{crit}}$ , black vertical line) and the range of angles where the modulation is of opposite sign for the two different thicknesses of fat (grey shaded area) are marked on the plot. (b) and (c) images of porcine tissue samples at visible (left) and 140 GHz (right) frequencies. (b) shows a large fatty region well separated from the protein, and (c) shows thin filaments of fat embedded in protein, while the regions of fat and protein are clearly distinguishable in both. The  $64 \times 64$  pixel mm-wave images are an average of 100 images taken with TE polarisation, where each took 4.1 seconds to collect (images collected over shorter times can be found in section 3.3 of the supplementary material).

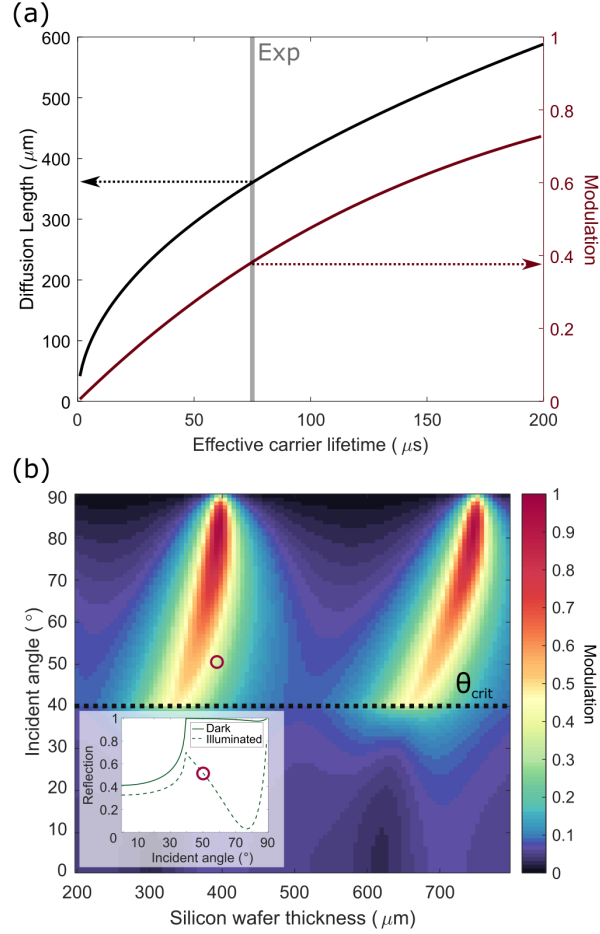


**Fig. 4.** (a) Calculated diffusion length of carriers (left, black axis) and modulation (right, red axis) as a function of effective charge carrier lifetime for a mm-wave beam incident at  $50^\circ$  through the prism material onto a  $390\ \mu\text{m}$  thick wafer. The grey line shows the lifetime of the wafer used in experiment. (b) TE polarised modulation of a mm-wave signal as function of angle of incidence in the prism material and silicon wafer thickness, assuming a charge carrier lifetime of  $75\ \mu\text{s}$ . Inset shows the reflection for dark and illuminated states for a  $390\ \mu\text{m}$  thick wafer. All results are calculated at  $140\ \text{GHz}$  mm-wave frequency, and an incident photoexcitation wavelength of  $623\ \text{nm}$  and power of  $220\ \text{Wm}^{-2}$  when illuminated, and  $0\ \text{Wm}^{-2}$  when dark. The red circles show the experimental parameters.

# Millimetre-wave total internal reflection based computational imaging - Supplementary Information

L. E. Barr, P. Karlsen, S. M. Hornett, I. R. Hooper, M. Mrnka,  
C. R. Lawrence, D. B. Phillips, E. Hendry

August 9, 2022

## 1 Introduction

In this supplementary material further details on the experimental design will be discussed, along with a deeper analysis of the images that are presented in the accompanying paper. Future works are explored, including thickness and optical parameter extraction from images, and imaging through opaque media.

## 2 Parameters of the system

### 2.1 Details of experimental setup

Since imaging in the mm-wave range is still a challenge we employ all-optical modulation (known as photomodulation), using a visible or near-IR light source to modulate the low frequency radiation source in a photo-active medium (such as silicon). We use light from a 4.7 W,  $623 \pm 5$  nm LED, which travels up through the transparent prism to the silicon wafer. This allows photoexcitation of the silicon wafer while keeping the top surface of the silicon free for samples. Using a digital micromirror device (DMD) from Vialux, we pattern the optical beam in order to locally modulate the photoconductivity in the silicon wafer. A light guide is used for homogeneous illumination of the DMD, and projection of the patterned light to our modulator occurs using a series of achromatic lenses (focal lengths 10 cm and 7.5 cm) and mirrors. We generate masks of spatially varying photoconductivity, which are imprinted on to the reflected mm-wave beam, providing the spatial information needed to construct an image using a single detector. We use a set of Hadamard masks, similar to [1, 2], which, when implemented correctly, can significantly boost the signal compared to conventional raster scanning [3]. As shown below, this approach provides good signal to noise in images while avoiding the complex image reconstruction calculations associated with compressive imaging techniques [3], allowing us to both measure and reconstruct the image in a few seconds. More details on the image reconstruction are given in section 3.1.

The majority of images shown in this paper are defined by  $64 \times 64$  pixels, requiring  $2 \times 64^2 = 8192$  masks to be generated, and the mm-wave signal collected for each one.

We collect the measurements at a frame rate of 2 kHz, so each image is recorded in 4 seconds. Images presented below are an average of 100 sequential image measurements. Images with smaller numbers of pixels or fewer averages can be collected in shorter times, and are presented in section 3.3 for comparison.

## 2.2 Wafer thickness

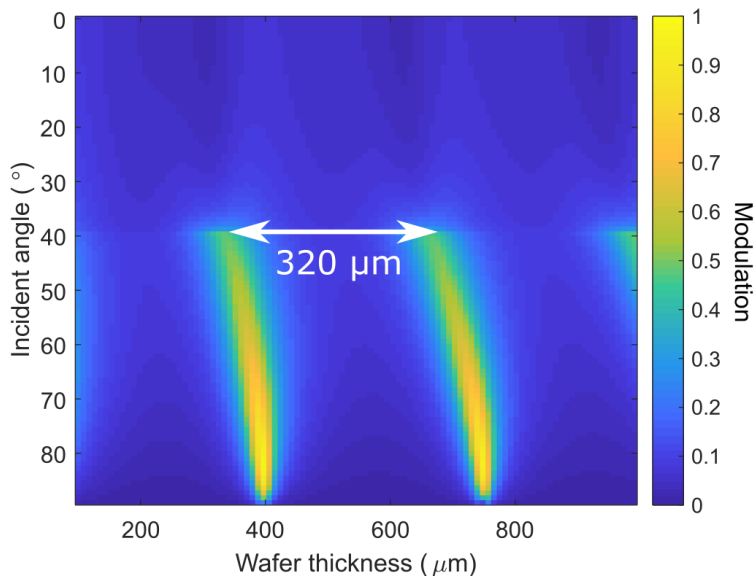


**Fig. S 1.** Simulated modulation assuming 140 GHz radiation incident on a wafer with a  $75 \mu\text{s}$  effective charge carrier lifetime and photoexcited by a 623 nm pump source of intensity  $200 \text{ Wm}^{-2}$ . The peaks in modulation are periodic with the wafer thickness, and suggest a Fabry-Perot cavity resonance in the wafer plays an important role on the modulation.

We mention in the main text that the thickness of the wafer is very important when designing the imaging system. Fig. S1 shows the modulation calculated for an incident wave of 140 GHz at various angles for various wafer thicknesses. Two clear peaks are shown with a separation of around  $320 \mu\text{m}$  at the critical angle, as shown by the white arrow. The refractive index of silicon is 3.42, therefore the wavelength of the mm-wave beam inside the silicon is  $625 \mu\text{m}$ . The peaks are separated by almost one half-wavelength, and shift to higher frequencies as the angle of the incident beam is increased. These are both behaviours that are characteristic of a Fabry-Perot resonance inside the silicon.

## 2.3 Frequency and incident angle

In Fig. S2 (a) we plot the modulation as a function of both incident angle and frequency. We see that the modulation for all frequencies with incident angles below  $\theta_{\text{crit}}$  (white dotted line) is small, but for larger angles the modulation is highly frequency dependent. We observe a peak in the modulation just above 140 GHz, which varies with the thickness of the silicon wafer, and is attributed to a resonant Fabry-Perot cavity mode inside the wafer (see Fig.

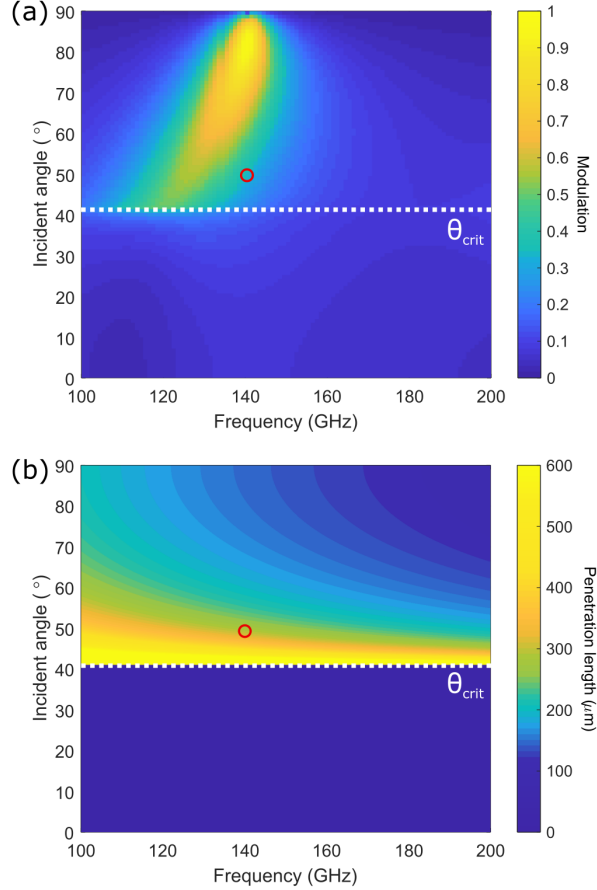


**Fig. S 2.** (a) Calculated modulation and (b) penetration length of evanescent fields at the silicon-air boundary as a function of both angle of incidence and frequency. The white dashed lines represent the critical angle above which total internal reflection occurs. The red circles highlight the set of parameters chosen for the experimental measurements.

S1. Near this resonant feature, and for TE polarisation with an angle of incidence around  $82^\circ$ , we predict a modulation depth of  $> 99\%$  with an optical illumination intensity of just  $220 \text{ Wm}^{-2}$ , achievable with a commercial LED source.

While matching the frequency to the silicon wafer thickness is beneficial to achieve the largest signals, one must also consider the thickness of the sample. When there is a dielectric medium above the silicon with a refractive index lower than that of the prism, the penetration length of the evanescent fields ( $L$ ) will determine the depth of material that can be probed. We plot

$$L = \frac{\lambda}{4\pi \sqrt{n_{\text{silicon}} \sin^2 \theta_{\text{silicon}} - n_{\text{sample}}^2}} \quad (1)$$

as a function of frequency and incident angle in the prism in Fig. S2 (b), assuming a sample index of 1.  $\theta_{\text{silicon}}$  is the angle of refraction in the silicon, and is related to the angle of incidence in the prism,  $\theta_{\text{prism}}$  via Snell's Law:  $\theta_{\text{silicon}} = \arcsin\left(\frac{n_{\text{prism}} \sin \theta_{\text{prism}}}{n_{\text{silicon}}}\right)$ . For

all frequencies and all angles below  $\theta_{\text{crit}}$  there are no evanescent fields at the silicon-air boundary. Above  $\theta_{\text{crit}}$  the penetration length is larger for lower frequencies and drops off towards higher frequencies. Thus, if we are interested in probing only the surface of a low-index sample, higher frequencies are more suitable. However, if one would like to probe the bulk of a sample, or even determine the thickness of layers, lower frequencies mean longer penetration of the fields into a sample. Hence, in practice, there is a trade off between the incident angles and frequencies which give the largest signals, and those that probe the bulk of the material in the half-space above the wafer. In the main text, we image tissue layers of a few hundred micron thickness, with refractive indices that are close to or higher than that of the prism. In this case the mm-wave beam is totally internally reflected from the sample-air boundary on the side furthest from the silicon, and instead the absorption and scattering of propagating waves inside the sample provide the contrast in the image. The red circles in Figs. S2 (a) and (b) represent the parameters selected for the experimental measurements - a frequency of 140 GHz (chosen from a limited selection of available sources and the proximity to the wafer cavity resonance) and incident angle of  $49^\circ$  (corresponding to a penetration depth of around  $300 \mu\text{m}$  in air). The experimentally determined modulation for this geometry is 69.9% which is higher than the theoretical predictions in Fig. S2 (a) of around 40%.

## 2.4 Measuring the effective charge carrier lifetime

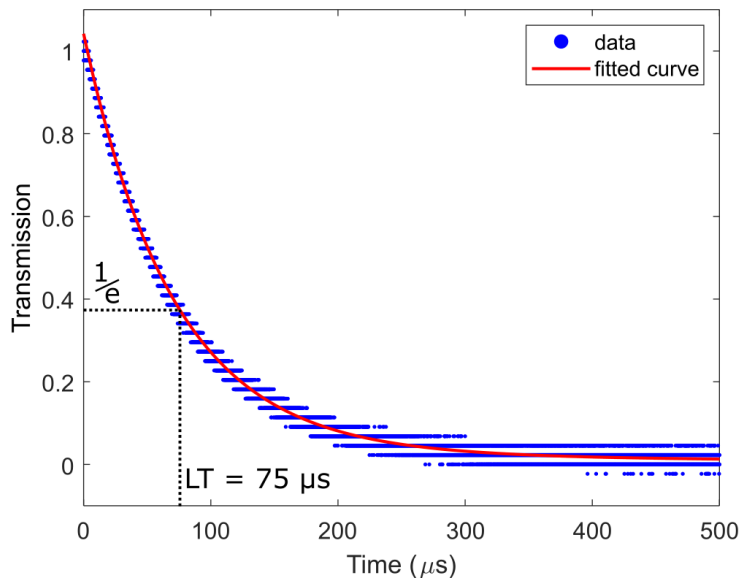


**Fig. S 3.** Plot of the normalised transmission of a 60 GHz signal through the  $390 \mu\text{m}$  thick wafer used in the experiment. The point where the intensity of the signal falls to  $1/e$  of the original is marked, and corresponds to an effective charge carrier lifetime of  $75 \mu\text{s}$ .

In order to measure the effective charge carrier lifetime of the wafer used for the photomodulator, the transmission through the wafer at 60 GHz was measured as a function of time as a photoexciting light source was modulated. Note that the lifetime of the charge

carriers is a property of the wafer and will not change as a function of frequency. The wafer was oriented at a  $45^\circ$  angle to a 1 ms TTL modulated photoexciting source (a collimated 4.8 W SOLIS-623C LED from Thorlabs with an output wavelength of 623 nm). The 60 GHz source was an Anritsu Vectorstar MS4647B Vector Network Analyser in CW mode with a Flann 25240 25 dB standard gain horn antenna, which was also oriented at  $45^\circ$  to the wafer, and orthogonal to the photoexciting light. The magnitude of the signal transmitted through the wafer was detected using a Sage Millimeter SFD-503753-15SF-P1 waveguide detector connected to an oscilloscope triggered from the modulated light source. The waveform of both switch on and switch off events were recorded for a range of photoexciting intensities. Fig. S3 shows the transmission through the wafer as a function of time (blue dots) and an exponential curve fitted to the data. The photoexciting source is switched on at time = 0, and the time elapsed when the signal has fallen to  $1/e$  of the original is taken to be the lifetime of the wafer, as marked by the black dashed lines.

## 2.5 Effect of charge carrier distribution

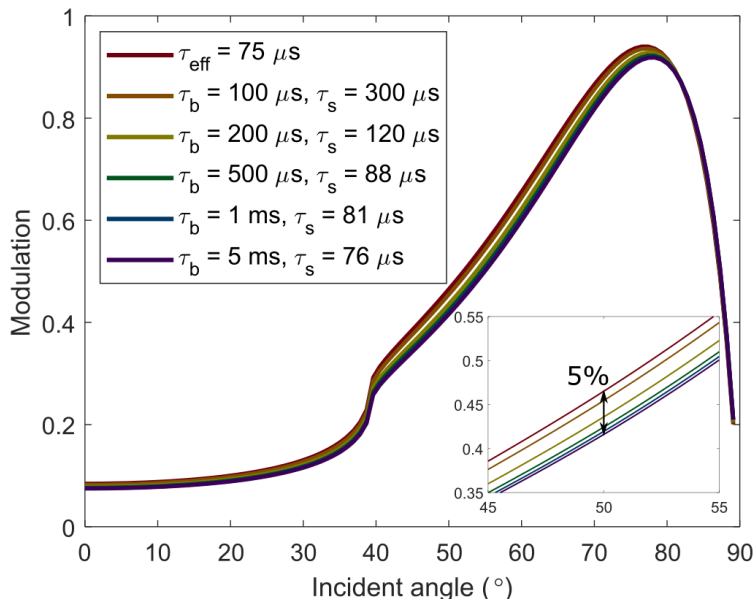


**Fig. S 4.** Simulated modulation of a  $390\ \mu\text{m}$  thick wafer with an effective lifetime of  $75\ \mu\text{s}$ . The red line assumes a uniform homogeneous charge carrier distribution, each of the other lines are calculated assuming different combinations of bulk and surface lifetimes that each lead to an effective lifetime of  $75\ \mu\text{s}$ . The inset shows a zoomed-in section that illustrates the small deviation in modulation for each wafer.

Throughout the analysis in the main text we assume that the modulation from the silicon wafer could be predicted reasonably well by assuming that the distribution of charge carriers is uniform across the wafer thickness. Under this assumption the modulation depth is proportional to the excess charge carrier density,  $\Delta n$ , which is dependent only on the effective lifetime of the carriers,  $\tau_{\text{eff}}$ , the excitation function,  $G$  (proportional to the intensity of the incident light) and the thickness,  $d$ , of the silicon wafer, according to  $\Delta n = \tau_{\text{eff}}G/d$ .

For modulators in a transmission geometry this approximation is very good, as the wave will travel through the entire wafer and be subject to the total amount of charge carriers. However in the total internal reflection geometry this approximation is not necessarily valid. Instead it may be more appropriate to separate the recombination of charge carriers into bulk,  $\tau_b$  and surface  $\tau_s$  contributions, which are related to the effective charge carrier lifetime via  $1/\tau_{\text{eff}} = 1/\tau_b + 1/\tau_s$ . However for comparison to the experiment we would need accurate measurements of bulk and surface lifetimes, and this is not a straightforward measurement to perform. Instead we can measure the effective lifetime (see figure 3) and use this value in the simulation. It is still pertinent to check that the assumption of effective lifetime is valid.

Fig. S4 shows the calculated modulation for wafers of various bulk,  $\tau_b$ , and surface,  $\tau_s$ , charge carrier lifetime. The distribution of charge carriers in silicon was found using a diffusion calculation, assuming illumination from one side. More details can be found in reference [4]. The red line represents a wafer with homogeneous charge carrier distribution, and assumes an effective charge carrier lifetime of 75  $\mu\text{s}$ . The following lines show the modulation expected from wafers that each have an effective charge carrier lifetime of 75  $\mu\text{s}$ , but which have different bulk and surface lifetimes. The charge carrier distribution will be most inhomogeneous in wafers with large bulk lifetimes and high surface recombination rates, which correspond to low surface lifetimes. This is the case where we would expect the maximum deviation in modulation from the homogeneous distribution. However for all lifetime combinations investigated here (which cover the typical values found in undoped silicon wafers), the difference in modulation between homogeneous and non-homogeneous distribution does not exceed 5%. We can therefore say that our approximation still leaves us with a reasonably valid model for the modulation, although we must be aware that there is a possibility the simulation will predict modulations slightly higher than those measured in experiment. It is also worth keeping in mind that if the wafer thickness was reduced this approximation becomes worse as the surface recombination rate becomes more dominant in determining the effective charge carrier lifetime.

## 3 Parameters for imaging

### 3.1 Orthonormal single-pixel computational imaging

Without photomodulation of the silicon wafer, the total internal reflection geometry results in the entire underside of the sample being immersed in a mm-wave field when the source is active. Inhomogeneities in the complex refractive index of the sample result in a spatial variation in the level of scattering of the evanescent field. Therefore, the intensity of totally internally reflected mm-wave radiation spatially varies in a sample dependent manner. In order to reconstruct an image of this spatial variation using only a single-element detector, we sequentially project a series of  $N$  patterns, each of which probes a different subset of the spatial information of the sample. In each case, the detector records the totally internally reflected signal  $a_n$ , which is proportional to the level of spatial overlap (i.e. dot product) between the scattering profile of the sample and the  $n^{\text{th}}$  displayed 2D pattern  $\mathbf{H}_n$ . If these patterns are chosen to be orthonormal, then the resulting image  $\mathbf{I}$  can be reconstructed from

a sum of the patterns, each weighted by the measured overlap with the sample:

$$\mathbf{I} = \sum_{n=1}^N a_n \mathbf{H}_n, \quad (2)$$

where  $\mathbf{I}$  represents a 2D image containing  $N$  pixels. In this case the patterns are drawn from the orthonormal Hadamard basis, similar to [1,2], which, significantly boosts the signal compared to a set of patterns equivalent to conventional raster scanning, as shown in [3]. In practice, use of the fully sampled Hadamard basis requires the display of  $2N$  patterns to ensure that the patterns are orthogonal, as described in [5].

### 3.2 Number of pixels

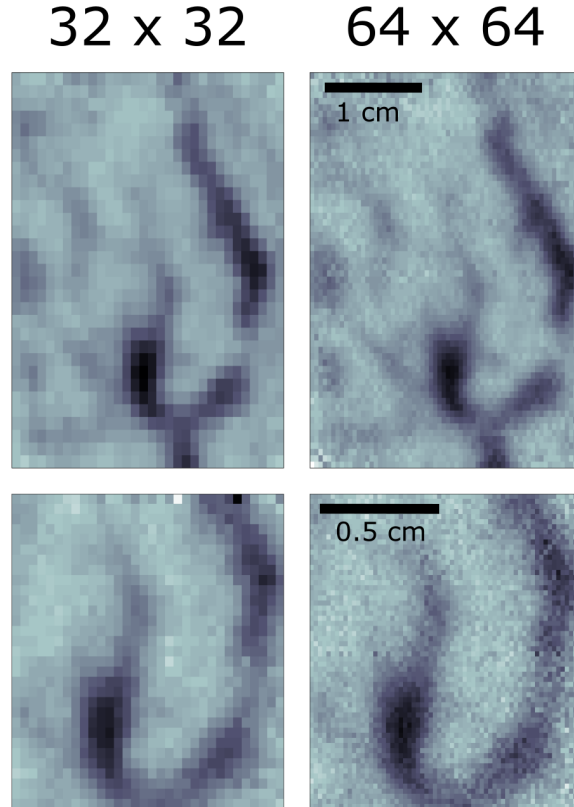


**Fig. S 5.** A comparison between images with  $32 \times 32$  pixels (left panels) and  $64 \times 64$  pixels (right panels), and a larger (top panels) and smaller (bottom panels) field of view.

When taking mm-wave images in the near-field we are able to select the field of view and the number of pixels of the image. Fig. S5 shows four images taken of the same porcine tissue sample with a larger (top row) and smaller (bottom row) field of view, and either  $32 \times 32$  (left) or  $64 \times 64$  (right) pixels. The darker areas are filaments of fat running through an area of protein.

Increasing the number of pixels does improve the clarity and resolution of the images, however this also leads to an increase in imaging time by a factor equal to twice the number of additional pixels. Reducing the field of view while maintaining the same number of pixels does not affect the time taken to collect images, and does allow finer structures in the sample to be seen more clearly. However reducing the field of view is done by decreasing the area of the digital micromirror device (DMD) that is used, and therefore reduces the portion of the mm-wave beam that is modulated and leads to an increase in the background signal. In extreme cases it will also limit the achievable resolution, as there needs to be as many micromirrors as pixels in the selected DMD region. Therefore when considering any application, careful thought should be given to the required speed and acceptable resolution, in order to decide on the most appropriate number of pixels.

### 3.3 Measurement time

Another parameter of the imaging system that can be tuned is the time over which the mm-wave signal is collected for each frame. Fig. S6 shows an array of images taken of the same porcine tissue sample at various frame rates and averages, all with  $32 \times 32$  pixels apart from the top row which has  $64 \times 64$  pixels, as indicated.

The signal to noise ratio is drastically improved by either increasing the number of averages taken, or decreasing the frame rate and increasing the signal collection time accordingly. We can investigate which of these methods is best for reducing the noise, as this depends on the nature of the noise itself. Taking only a few averages of signals collected over a long time with a low frame rate will effectively eliminate noise that is quickly varying. However if the noise in the system is varying slowly with time, it is more effectively minimised by increasing the number of averages taken for each frame.

In this system, when comparing two images that have equivalent total collection times (e.g. 20 averages at 2 kHz and 5 averages at 0.5 kHz), it can be seen that the high frame rate/high averaging option gives a signal to noise ratio that is slightly better than the low frame rate/low averaging option, although they are both very similar.

### 3.4 Polarisation

One other parameter at our disposal is the polarisation of the mm-wave beam we are using. The calculation presented in Fig. S7 (a) shows that, for an air sample, much larger modulation is expected for TE polarisation than for TM. This should lead to greater contrast in images, and improved signal-to-noise ratios.

To illustrate this, Fig. S7 (b) shows two images of porcine tissue taken with identical measurement parameters, but with opposite linear polarisations. It is clear that the contrast and signal-to-noise ratio are greatly improved for the TE polarisation compared to the TM.

## 4 Analysis of images

In this section we will analyse some possible sources of artefacts arising from the imaging process, such as diffraction of mm-wave beam from the masks and the use of Hadamard

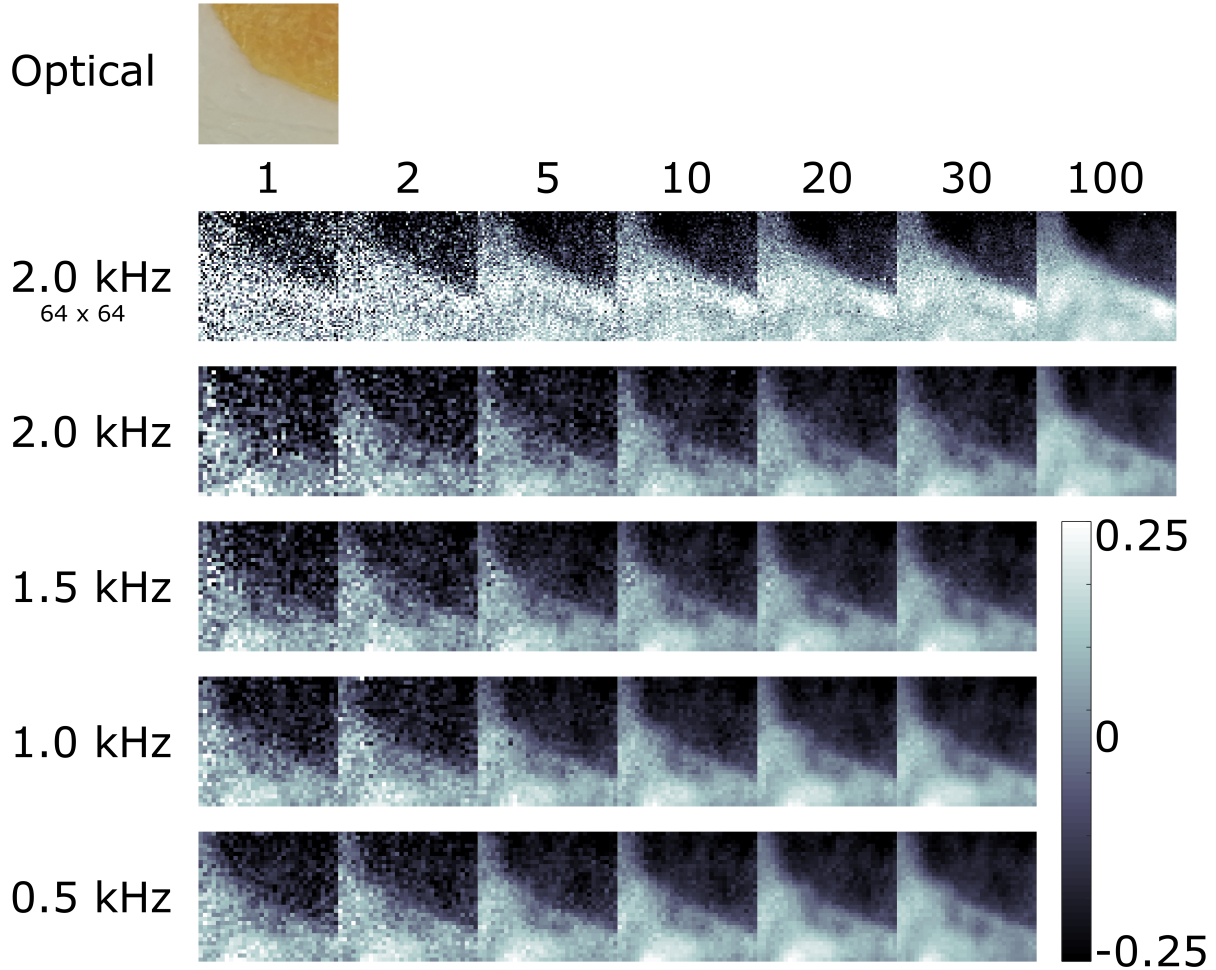


**Fig. S 6.** A selection of images taken of the same porcine tissue sample (optical image at top) taken with different imaging parameters. Rows contain images with the same frame rate, and columns contain images with the same averages. In the very top row the images have  $64 \times 64$  pixels, all others have  $32 \times 32$  pixels.

masks. We will also discuss in more detail the interpretation of the information held in each image, including the extraction of material parameters and thickness of samples. Finally, we will present evidence of imaging objects hidden behind a layer of biological tissue.

#### 4.1 Diffraction from mask

A fundamental part of our imaging technique requires periodic structures in the conductivity of the silicon to be created. For some of the masks in the Hadamard set, these can be of a similar size to the wavelength. Therefore for these masks there will be some diffraction of the mm-wave beam that is reflected off this structured surface. It could be suggested that this will lead to artefacts in the images, and so is worth looking at in more detail.

Fig. S8 (a) shows how the mm-wave signal measured by the detector changes as a function of angle. For the measurement, the source detector and mm-wave lens were positioned as

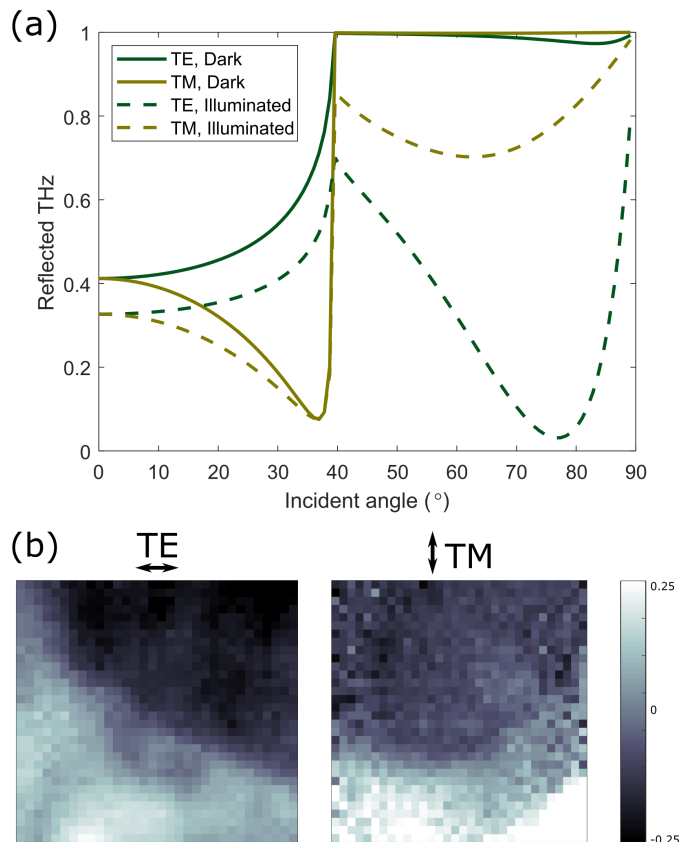


**Fig. S 7.** (a) Calculated reflection at 140 GHz from a 390 μm thick silicon wafer with a 75 μs charge carrier lifetime on a half-space of prism material (TPX polymer), as a function of incident angle for both TE and TM polarisations. In the dark state there is no photoexcitation, and in the bright state a 623 nm optical beam is incident on the wafer with an intensity of 220 W/m<sup>2</sup>. (b) Comparison between images taken with the same imaging parameters but with different polarisations, represented by the arrows above each image.

they were in the imaging system. The source was modulated at 1 kHz and the signal from the detector recorded with a lock-in amplifier for each angle as the source was rotated about the exit aperture. It is seen from Fig. S8 (a) that the signal has significantly reduced to less than 20% at angles greater than  $\pm 10^\circ$  from normal incidence.

Figs. S8 (b) - (d) show how this angular response compares to typical angles of diffraction from a selection of Hadamard masks, shown in the inset in each plot. To obtain these, a 2-dimensional fast Fourier transform was taken of the electric field at the surface of each mask, assuming that it is projected over an area of 25 mm<sup>2</sup>, and for a frequency of 140 GHz. A slice is taken through the centre of the 2-dimensional plot for comparison. Only masks with 1-dimensional structure have been presented here for simplicity, but this technique can be applied to all masks, as diffraction along the y-axis has the same behaviour as diffraction along the x-axis.

Panel (b) in Fig. S8 shows the Fourier transform of a mask with relatively coarse structure, which is one of very few that will produce diffracted orders within the acceptance

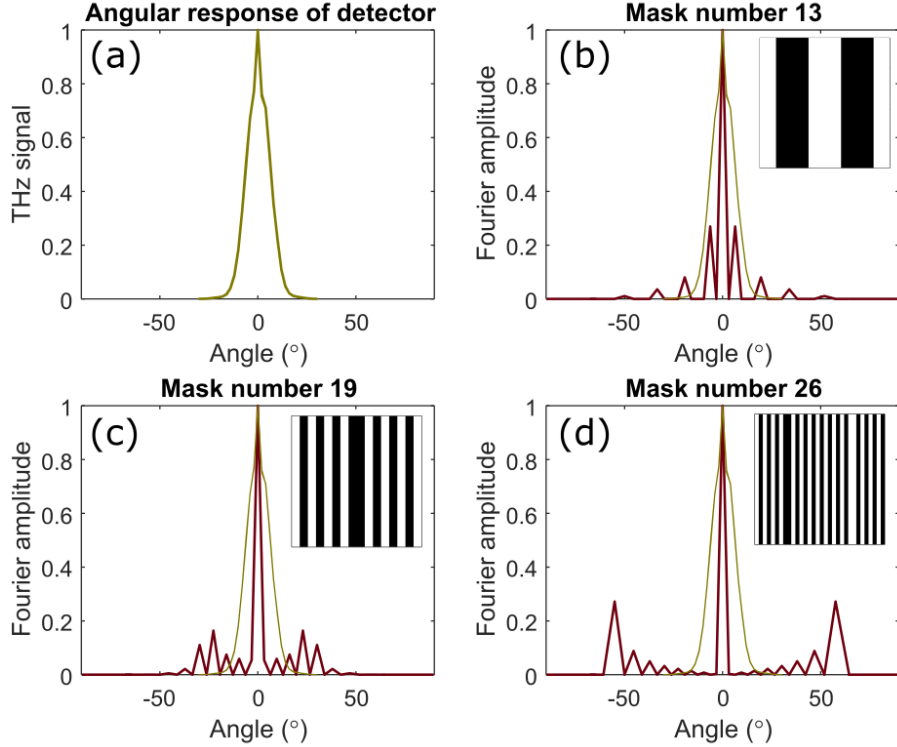


**Fig. S 8.** (a) shows the measured angular response of the detector. (b), (c) and (d) show the calculated diffraction pattern of a 140 GHz beam that is travelling through the prism material and reflected from a Hadamard mask shown in the inset. Coarse structured masks lead to some diffracted orders falling inside the detection range of the detector, but most masks have fine structures and the diffracted beams cannot be detected in the set-up.

angle of the detector. In this case, the first diffracted order will be detected when imaging. However, as the masks become finer and more sub-wavelength in structure, such as those in panels (c) and (d), the beams are diffracted at higher angles and will not be recorded by the detector. We can say that the majority of masks have a structure that is sufficiently sub-wavelength that the diffracted orders will not interfere with collected signals.

It is also worthwhile considering the fact that the total power that can be diffracted into any of the higher orders is very limited. Ignoring the diffusion of charge carriers, and the less than 100% modulation, the masks can be approximated as a square-profile amplitude grating. The diffraction efficiency depends on the duty cycle of the grating, which will vary for different masks, and is highest for a 50% duty cycle grating. According to calculations performed here [6], at most 10.1% of the total power can be diffracted into the first order mode, and will decrease for duty cycles other than 50% and for less than 100% modulation, and further due to the smearing of the square profile due to charge carrier diffusion. Taking into account the angles and efficiency of diffraction, for the majority of the masks used in the imaging process, collection of diffracted beams is not a likely cause of artefacts in the images that we collect. The masks that may be affected by diffraction are those with very coarse structure, and if this was a significant effect we would clearly see a coarse structure over the images, and we do not.

## 4.2 Simulation of imaging

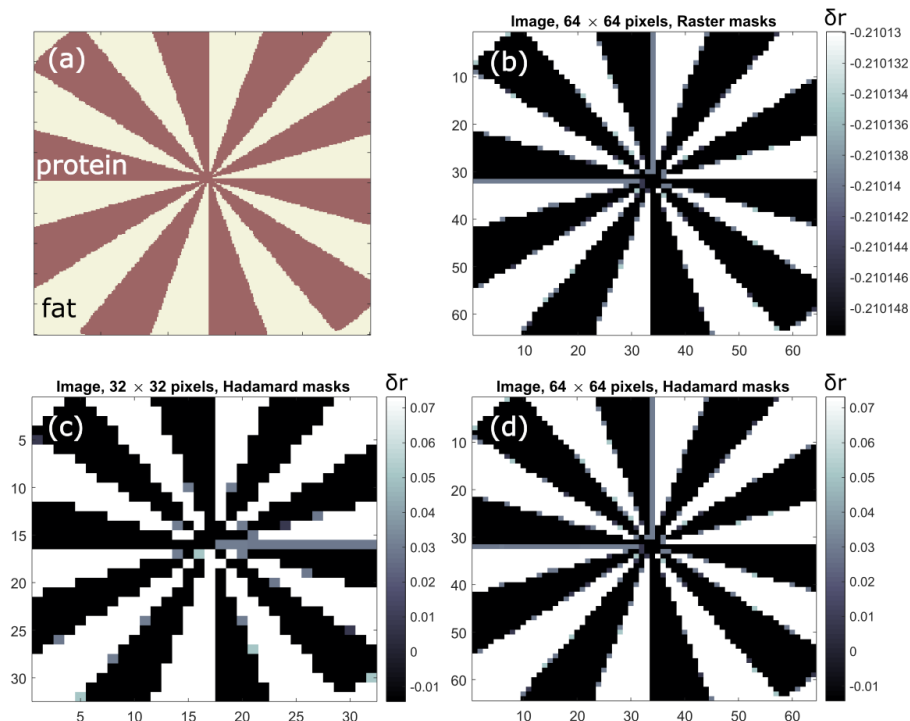


**Fig. S 9.** Results of simulation of imaging a Siemens star. The original object is in panel (a), (b) shows an image taken with a  $64 \times 64$  raster scan, (d) shows an image taken with a  $32 \times 32$  pixel Hadamard scan, and (c) shows an image taken with a  $64 \times 64$  pixel Hadamard scan.

Another possible cause of unusual features in the images could be artefacts arising from the use of Hadamard masks themselves. In order to investigate this, a simulation of the imaging was created based on the analytical methods described in [4].

A transfer matrix code is used to calculate the reflection from an infinitely large area of several different stacks that are possible in the imaging system, i.e. combinations of illuminated or dark silicon, and protein or fat samples. These values are assigned to each pixel of a mask, and for mask pixels that cover regions with both fat and protein, linear interpolation between reflection coefficients is used. An arbitrary binary pattern of fat and protein regions is drawn. This is then overlaid with a Hadamard matrix, and the material in each pixel is used to select the reflection coefficients for dark and illuminated silicon. The reflection coefficients for each pixel are added and normalised to find the total reflected signal from that mask, which is then used in the reconstruction in the same way as in the experiment to find the value of  $\delta r$ .  $\delta r$  is the difference in reflection when the modulator is on (illuminated) and off (dark), similar to the modulation but with a sample in place. This is repeated for all masks in the set, and to obtain a true comparison with experiment, the matrices are separated into positive (i.e. in the Hadamard matrix +1s become 1s and -1s become 0s) and negative masks (i.e. +1s become 0s and -1s become 1s) in the simulation as well.

This model is a very simple approximation of what is happening in the imaging. It does not take into account any effects due to diffraction of the mm-wave beam by the mask or the sample, and any resonances in the plane of the sample will not be reproduced, as each pixel is assumed to be infinitely large and not interacting with the neighbouring pixels. However it is still a useful tool for interpreting images and predicting the effects of sample index and thickness.

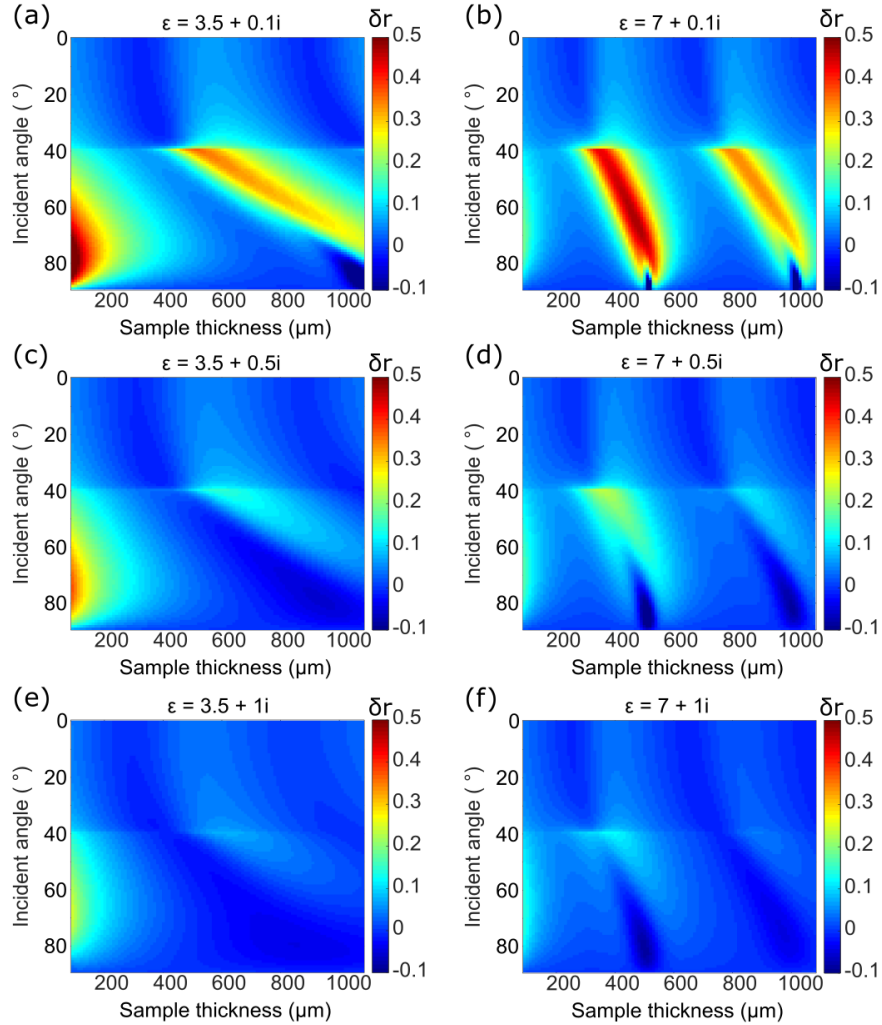


**Fig. S 10.** Plots of simulated  $\delta r$  as a function of sample thickness and incident angle of the mm-wave beam. All results are calculated at 140 GHz mm-wave frequency for a 390  $\mu\text{m}$  thick silicon wafer with a charge carrier lifetime of 75  $\mu\text{s}$ , and an incident photoexcitation wavelength of 623 nm and power of 220  $\text{Wm}^{-2}$  when illuminated. The samples in each column have the same real permittivity, and in each row the imaginary permittivity is the same.

Fig. S9 shows the result of a simulation of a fat and protein sample. The thickness of the sample is 700  $\mu\text{m}$ , and the material parameters for fat and protein are the same as in the main text, along with all other experimental parameters. The object being imaged, (a),

is a Siemens star made of arms of fat (cream) and protein (pink). The image in panel (b) was taken using a simulated raster scan, (c) using a lower resolution simulated Hadamard scan, and (d) using a simulated Hadamard scan with the same resolution as (b). It is clear that the magnitude of signals collected is much larger when using Hadamard masks over Raster scanning, and also that the resolution is reduced when the number of pixels is reduced. However, in all images there are no features or artefacts that arise from the use of Hadamard masks.

### 4.3 Sample losses and critical coupling

It is explained in the main text of the paper that a change in sign of an image is due to a change in sign of the  $\delta r$ . This is proposed to be due to meeting the condition for critical coupling, where absorption of the mm-wave beam will be most efficient. This is achieved when the damping coefficients for radiative and non-radiative loss mechanisms are equal [7], and is due to a Fabry-Perot resonance in the thickness of the sample. This condition, rather counter-intuitively, can be reached by reducing the losses in the silicon wafer, and lead to a situation where more of the mm-wave is absorbed when the silicon is not illuminated. If this is a correct interpretation, we expect that the losses in the sample will play an important role in reaching this condition. We propose that it will also depend on a resonance determined by the thickness and index of the sample, which provides the radiative loss component. In this section we explore the parameter space, and look at how the  $\delta r$  changes with real and imaginary parts of the permittivity of the sample.

Fig. S10 shows the  $\delta r$  as a function of the incident angle and sample thickness for a range of real and imaginary permittivities. The sample that is closest to the experimental example in the main text is (c). Comparing (a) and (b), we see that changing the real part of the permittivity changes the sample thickness at which the resonant condition is met, and shifts the resonant peak in  $\delta r$  to lower thicknesses for higher indices, as well as reducing the angular dispersion. These are both features of a Fabry-Perot type cavity resonance in the sample. However, due to the low losses in the sample in (a) and (b), we do not observe any negative  $\delta r$  below very high incident angles. Increasing the loss, as in (c) and (d), introduces a range of thicknesses where the  $\delta r$  is negative, followed by a range of sample thicknesses that give positive  $\delta r$ . Again the real part of the permittivity effects the thickness and angle where this is observed. Finally, in (e) and (f), the losses are increased again, and the magnitude of the positive  $\delta r$  drops in general, while there is still a region where negative  $\delta r$  can be observed.

### 4.4 Variation in tissue properties

There are varying values for the permittivity of biological tissues reported in the literature. For the analysis conducted in this work we use values reported by Gabriel et al [8], where the complex permittivities are  $\epsilon_{\text{fat}} = 2.89 + 0.64i$  and  $\epsilon_{\text{protein}} = 8.63 + 11.20i$ . Fig. S11 (a) and (b) show the  $\delta r$  calculated as a function of incident angle and sample thickness for layers of protein and fat respectively, assuming these permittivities. However, there are wide ranges of values reported for the complex permittivities of fat and protein in the literature [8–12]. As an example, Bowman et al [9] report a different value for the permittivity of protein,  $\epsilon_{\text{protein}} = 8.28 + 5.10i$ . Note in particular the discrepancy between the losses in values

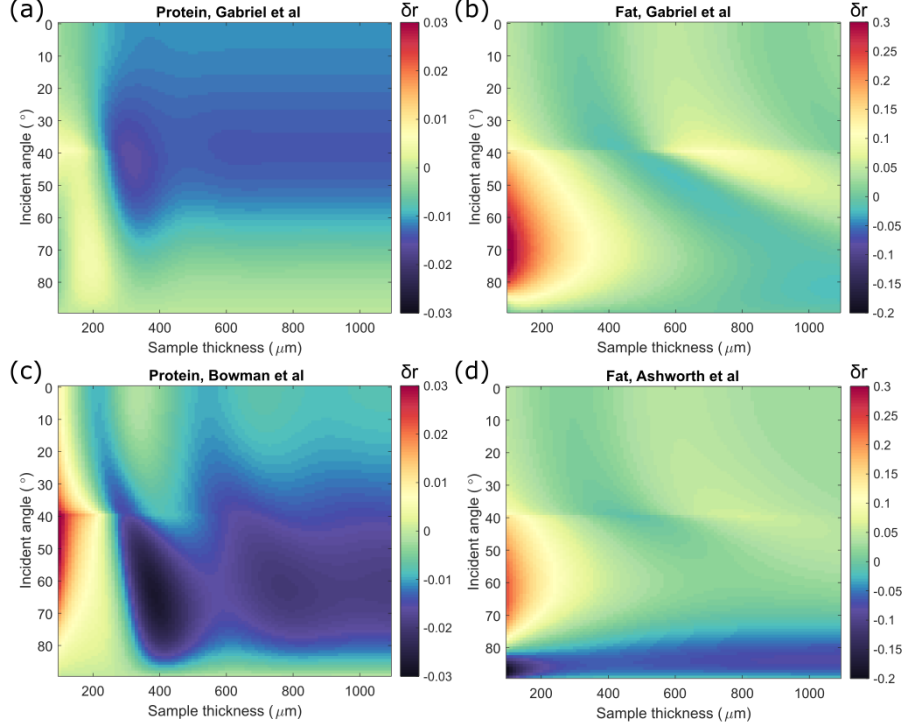


**Fig. S 11.** Calculated  $\delta r$  as a function sample thickness and incident angle for protein (panels (a) and (c)) and fat (panels (b) and (d)) samples, with permittivities taken from reference [8] (panels(a) and (b)), [9] (panel (C)) and [10] (panels (d)). All results are calculated at 140 GHz mm-wave frequency for a 390  $\mu\text{m}$  thick silicon wafer with a charge carrier lifetime of 75  $\mu\text{s}$ , and an incident photoexcitation wavelength of 623 nm and power of 220  $\text{W}/\text{m}^2$  when illuminated.

reported by both references. Fig. S11 (c) shows the calculated  $\delta r$  as a function of sample thickness and incident angle for protein, assuming the material properties from Bowman et al [9]. The effect of the lower losses given by Bowman et al is evident from the general increase in the magnitude of the  $\delta r$ , as well as the stronger dependence on the sample thickness, as there is less absorption of the mm-wave beam.

It is also worth noting that in reference [10], Ashworth et al state a real part of the permittivity of fat that is just below that of our prism ( $\epsilon_{\text{prism}} = 2.5 > \epsilon_{\text{fat}} = 2.29 + 1.05i$ ). In this case, the contrast mechanism for the imaging changes slightly, as the mm-wave is now reflected from the silicon-sample boundary at high incident angles. Fig. S11 (d) shows the  $\delta r$  calculated using this permittivity. By comparison with Fig. S11 (b) we see that the magnitude of the  $\delta r$  decreases, as the imaginary part of the permittivity given by Ashworth et al is higher. In addition, a band of large negative  $\delta r$  at high angles is seen. This is indicative of evanescently decaying fields inside the sample, which are very sensitive to the material parameters, but not to the thickness.

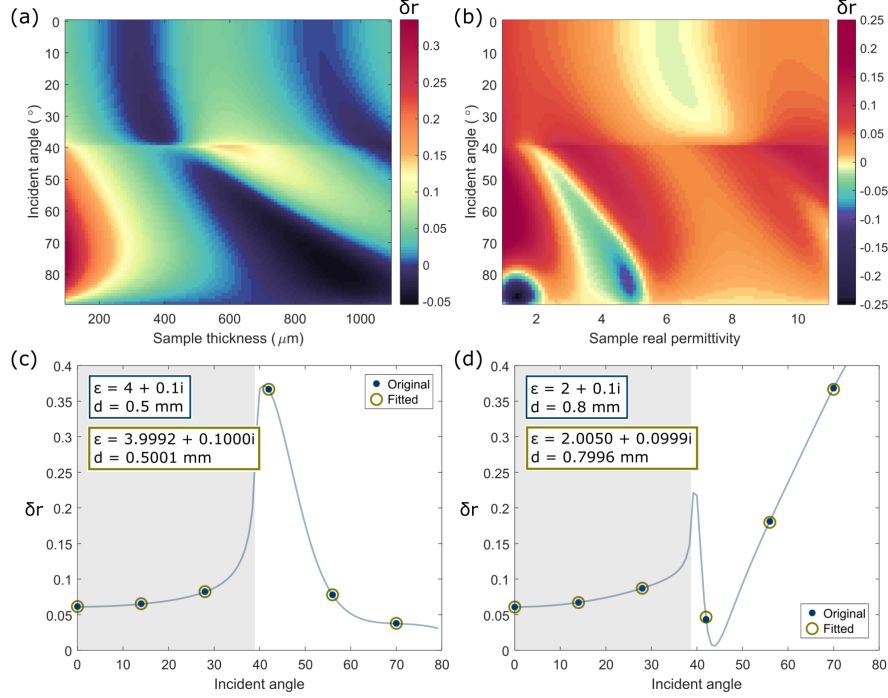


**Fig. S 12.** (a) Calculated  $\delta r$  as a function sample thickness and incident angle, for a sample with permittivity  $\epsilon = 3.5 + 0.525i$ . (b) Calculated  $\delta r$  as a function of the real part of the sample permittivity and incident angle, for a 500  $\mu\text{m}$  thick sample with imaginary permittivity  $\epsilon_i = 0.525$ . (c) and (d) Calculated (blue line, blue circles show the points chosen for fitting)  $\delta r$  for a sample with material parameters listed in blue inset box, and the  $\delta r$  calculated using the fitted material parameters in the yellow inset box (yellow circles). The grey shaded region shows the range of angles below the critical angle.

## 4.5 Extracting parameters

As mentioned in the main text, the ability to extract the permittivity and thickness of a sample from an image would open the door to many applications. Fig. S10 also gives us another insight, as we can see that the real and imaginary parts of the sample permittivity change the  $\delta r$  in independent ways. In other words, in any of the plots in Fig. S10, any vertical slice of data taken will not be identical to the same slice in any other, with particularly large contrast at higher angles. This suggests that, if we were able to collect enough information, it is possible to determine the complex permittivity of a sample. Furthermore, Fig. S12 (a) and (b) show that the permittivity and thickness of the sample affect the  $\delta r$  in non-identical ways. We can show that it is in fact possible to extract the complex permittivity and thickness of a sample from the  $\delta r$ .

Figs. S12 (c) and (d) show the results of two such extractions from simulated data, for two different samples. The inset blue box contains the expected parameters, and the blue circles on the plot correspond to the  $\delta r$  calculated from that sample at 6 different angles. The  $\delta r$  was then used in a non-linear least-squares fitting algorithm, and the parameters that we found as a result of the fitting are in the yellow box inset in each plot. The fitted  $\delta r$  is also shown by the yellow circles.

In both cases the fit is very good, and we are able to extract accurate values for the thickness, and real and imaginary parts of the permittivity simultaneously. While six data points have been given to this fitting routine, in theory only three points are needed to extract the three parameters. Adding more data reduces the chances of finding a local minimum, which is always possible. In addition, if fitting to experimental data, noise can introduce some uncertainty and means local minima are less easy to avoid. However more complex and robust fitting routines can be used to help avoid this, such as genetic algorithms, simulated annealing or swarm optimisation.

## 4.6 Imaging through tissue

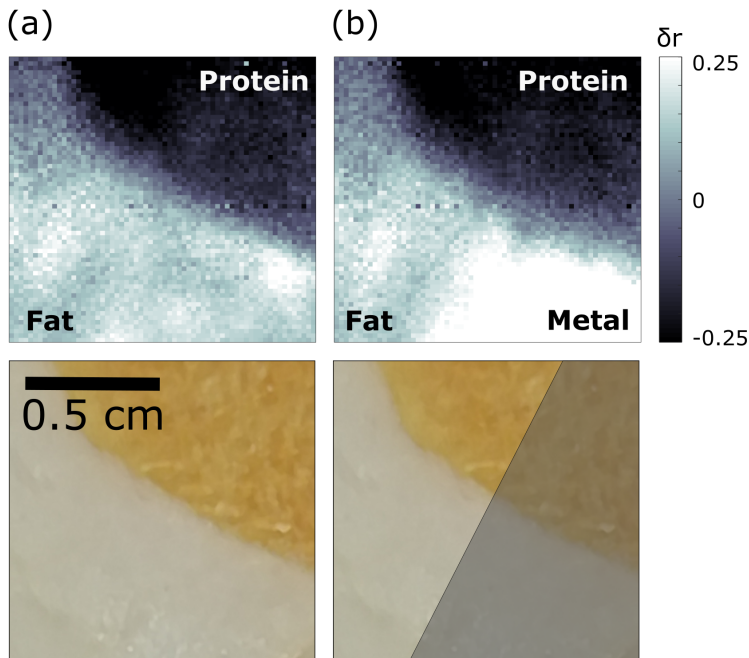


**Fig. S 13.** Visible (bottom row) and mm-wave (top row) images of the same sample of porcine tissue. (a) shows the sample in isolation, and in (b) a rigid strip of metal was placed on the far side of the sample, covering regions of both fat and protein. The metal is visible in the mm-wave image through fatty tissue but not through the protein due to the high mm-wave absorption. Both  $64 \times 64$  pixel mm-wave images were taken at 140 GHz using TE polarisation, and are averages of 100 images that took 4.1 seconds each to collect.

We present one final demonstration of near-field imaging using a TIR photomodulator, in which we image a metal object on the far side of a thin porcine tissue sample. This is shown in Fig. S13, using the same experimental parameters as described in the main text. Fig. S13 (a) shows the porcine tissue with only air on the top side, whereas in Fig. S13 (b) a rigid metal strip (shaded region in optical image) has been placed behind the tissue, on the opposite side to the modulator. In the region where the metal strip is behind the protein it cannot be observed, as the mm-wave is heavily absorbed within the protein, and the TIR wave is not strongly reflected due to the large real permittivity of protein. However

the metal is clearly visible as an increase in the reflected mm-wave in the fatty tissue region, seen by comparison to Fig. S13 (a). This demonstrates that it is possible to see through a thin layer of fat and observe objects behind it using a TIR mm-wave imaging technique.

## References

- [1] W. K. Pratt, J. Kane, and Harry C. Andrews. Hadamard transform image coding. *Proc. IEEE*, 57(1):58–68, 1969.
- [2] N J Sloane and M Harwit. Masks for Hadamard transform optics, and weighing designs. *Applied optics*, 15(1):107–114, 1976.
- [3] Rayko Ivanov Stantchev, Baoqing Sun, Sam M. Hornett, Peter A. Hobson, Graham M. Gibson, Miles J. Padgett, and Euan Hendry. Noninvasive, near-field terahertz imaging of hidden objects using a single-pixel detector. *Science Advances*, 2(6):1600190, 2016.
- [4] I. R. Hooper, N. E. Grant, L. E. Barr, S. M. Hornett, J. D. Murphy, and E. Hendry. High efficiency photomodulators for millimeter wave and THz radiation. *Scientific Reports*, 9(1):1–10, 2019.
- [5] Graham M. Gibson, Baoqing Sun, Matthew P. Edgar, David B. Phillips, Nils Hempler, Gareth T. Maker, Graeme P. A. Malcolm, and Miles J. Padgett. Real-time imaging of methane gas leaks using a single-pixel camera. *Optics Express*, 25(4):2999, 2017.
- [6] James E. Harvey and Richard N. Pfisterer. Understanding diffraction grating behavior: including conical diffraction and Rayleigh anomalies from transmission gratings. *Optical Engineering*, 58(08):1, 2019.
- [7] S. Herminghaus, M. Klopffleisch, and H. J. Schmidt. Attenuated total reflectance as a quantum interference phenomenon. *Optics Letters*, 19(4):293, 1994.
- [8] Camelia Gabriel. Compilation of the Dielectric Properties of Body Tissues at RF and Microwave Frequencies. Technical report, 1996.
- [9] Tyler Bowman, Magda El-Shenawee, and Lucas K. Campbell. Terahertz transmission vs reflection imaging and model-based characterization for excised breast carcinomas. *Biomedical Optics Express*, 7(9):3756, 2016.
- [10] Philip C. Ashworth, Emma Pickwell-MacPherson, Elena Provenzano, Sarah E. Pinder, Anand D. Purushotham, Michael Pepper, and Vincent P. Wallace. Terahertz pulsed spectroscopy of freshly excised human breast cancer. *Optics Express*, 17(15):12444, 2009.
- [11] Yiwen Sun, Bernd M. Fischer, and Emma Pickwell-MacPherson. Effects of formalin fixing on the terahertz properties of biological tissues. *Journal of Biomedical Optics*, 14(6):064017, 2009.

- [12] Yiwen Sun. A promising diagnostic method: Terahertz pulsed imaging and spectroscopy. *World Journal of Radiology*, 3(3):55, 2011.